



Instability and growth of nanoscale $\text{Ce}_{0.8}\text{Gd}_{0.2}\text{O}_{1.9}/\text{NiO}$ infiltrate in $\text{Sr}_{0.94}\text{Ti}_{0.9}\text{Nb}_{0.1}\text{O}_3-\text{Zr}_{0.84}\text{Y}_{0.16}\text{O}_{1.92}$ anodes for solid oxide fuel cells

Wei Zhang*, Luise Theil Kuhn, Peter Stanley Jørgensen, Bhaskar Reddy Sudireddy, Janet Jonna Bentzen, Carlos Bernuy-Lopez¹, Sune Veltzé, Tânia Ramos

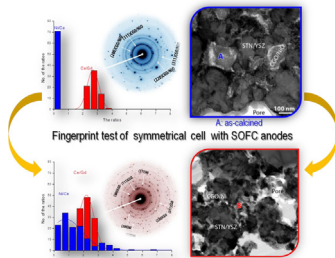
Department of Energy Conversion and Storage, Technical University of Denmark, 4000 Roskilde, Denmark



HIGHLIGHTS

- Nanoscale infiltration of ceramic anodes for SOFCs was performed.
- Structure evolution of nanoscale infiltrates under a variety of $\text{H}_2\text{O}/\text{H}_2$ atmospheres.
- Mechanism for instability of CGO/NiO nanostructures is discussed.

GRAPHICAL ABSTRACT



ARTICLE INFO

Article history:

Received 19 December 2013

Received in revised form

31 January 2014

Accepted 6 February 2014

Available online 20 February 2014

Keywords:

SOFC
Anodes
Infiltrate
Gd-doped ceria
Nickel
Instability

ABSTRACT

Microstructural evolution of $\text{Ce}_{0.8}\text{Gd}_{0.2}\text{O}_{1.9}/\text{NiO}$ (CGO/NiO) co-infiltrated nanoparticles in $\text{Sr}_{0.94}\text{Ti}_{0.9}\text{Nb}_{0.1}\text{O}_3-\text{Zr}_{0.84}\text{Y}_{0.16}\text{O}_{1.92}$ (STN94–YSZ) anodes for solid oxide fuel cells (SOFCs) is investigated during electrochemical testing in a symmetric cell setup. The CGO/NiO infiltrated symmetric cells were subjected to varying atmospheres of $\text{H}_2\text{O}/\text{H}_2$ between 650 and 850 °C and characterized by electrochemical impedance spectroscopy. Analytical high resolution transmission electron microscopy showed that the CGO/NiO infiltrate was found to coalesce and grow from an indistinguishable CGO/NiO fluorite structure of an average diameter of 5 nm to individual well-connected, but phase-separated, CGO and Ni particles of 50 nm in average. This study confirms that instability and growth of CGO/NiO infiltrates in STN-based SOFC electrodes affect the morphology and can potentially be linked to reported losses in electrochemical performance.

© 2014 Elsevier B.V. All rights reserved.

1. Introduction

A solid oxide fuel cell (SOFC) is one of the most efficient approaches for direct conversion of chemical energy into electrical energy [1–3]. A key step in the energy conversion in an SOFC is the

electro-oxidation of a fuel at the anode [4]. Infiltration of nanoscale electrocatalysts has become increasingly used in SOFC anodes [5,6], mostly to enhance important properties such as electrocatalytic activity for fuel oxidation. CeO_2 -based nanomaterials have received intensive attention as they have beneficial chemical and electrochemical properties [7]. Nanosized Gd-doped CeO_2 (CGO)/Ni infiltrate has been found to be an effective electrocatalyst, greatly enhancing the electrocatalytic activity for fuel oxidation in SOFCs [8–11]. One important concern is thereof raised: how stable is the nanoscale structure and related properties of the infiltrated

* Corresponding author.

E-mail addresses: phdweizhang@gmail.com, wzha@dtu.dk (W. Zhang).

¹ Present address: CIC EnergiGUNE, Parque Tecnológico de Álava, Albert Einstein 48, 01510 Miñano, Spain.

electrocatalysts under a variety of fuel environments and temperatures, relevant for SOFC operation, and what conditions can lead to instabilities? CGO/Ni potential stability issues have been previously raised for ceramic SOFC anodes in symmetrical cell configuration, upon exposure to high steam/high temperatures. In most cases, electrode performance degradation is addressed with detailed microstructural investigations, as determining microstructural evolution is of fundamental importance to understand the behavior of the electrochemical responses [12,13]. Thus, an accurate description of the microstructural evolution of the infiltrates may help improve selection of materials, facilitate evaluation of SOFC performance and help optimize electrode design.

Perovskite-based doped strontium titanate materials such as La-doped SrTiO_3 [14,15] and Nb-doped SrTiO_3 [16,17] have attracted a great deal of attention, ascribed to their good electronic conductivity at usual SOFC operating temperatures (over 100 S cm^{-1} in H_2 for dense, heavily reduced materials) in bulk materials. In this study, the microstructural investigations are focused on the stability and growth behavior of nanoscale $\text{Ce}_{0.8}\text{Gd}_{0.2}\text{O}_{1.9}/\text{NiO}$ particles co-infiltrated into symmetric cells of STN94/8YSZ composite SOFC anode backbones, which are subjected to a subsequent electrochemical testing (fingerprint). The objective of this paper is to show a detailed microstructure evolution of the CGO/NiO infiltrates in a variety of test environments in order to broaden our understanding of structural stability of electrocatalysts in SOFCs.

2. Experimental

2.1. Fabrication and electrochemical testing of symmetric cell

The symmetric cell production details can be found elsewhere [18,19]. In brief, the symmetric cells used in this work were a Sc_2O_3 and Y_2O_3 co-stabilized ZrO_2 electrolyte (180 μm thick), and two hand-sprayed composite electrode backbones of STN94–(10 vol.%) 8YSZ with an average thickness of 26 μm . The backbones were infiltrated using a suitable water-based solution of CGO/NiO precursor. The infiltration solution was prepared by dissolving the corresponding nitrates (Alfa Aesar, $\text{Ce}(\text{NO}_3)_3 \cdot 6\text{H}_2\text{O}$, $\text{Gd}(\text{NO}_3)_3 \cdot 6\text{H}_2\text{O}$, $\text{Ni}(\text{NO}_3)_2 \cdot 6\text{H}_2\text{O}$) in water along with a suitable surfactant (the nominal composition of CGO:Ni (in wt.%) is 90:10). Each backbone was infiltrated 2–3 times with an intermediate and final calcination in air at 350 °C for 2 h. One infiltrated and 350 °C calcined sample, Sample I, was kept as reference.

The other infiltrated symmetric cells were subjected to fingerprint protocol (see Refs. [18,19] for further details) in a specially designed test rig. The cells underwent an initial stay in air at 850 °C for 30 min, followed by a 9% H_2/N_2 atmosphere at 850 °C for 1 h. The cells were then characterized by electrochemical impedance spectroscopy (EIS) from 850 °C to 650 °C in 3% $\text{H}_2\text{O}/\text{H}_2$ (total 2 h, low pH_2O regime), followed by a warm-up to 850 °C in the same atmosphere. A further set of EIS measurements were then performed between 850 and 650 °C in 50% $\text{H}_2\text{O}/\text{H}_2$ (total 2 h, high pH_2O regime, Controlled via a pO_2 sensor at the gas-inlet). The sample that experienced the fingerprint is denoted Sample II.

In order to further infer on preliminary results, two additional samples were also analyzed. They have similar fabrication history as the aforementioned samples. After calcination at 350 °C, Sample I' underwent a stay in air at 850 °C for 2 h; while Sample I'' underwent a stay at 850 °C for 2 h using 9% H_2/N_2 . The history of the four samples is summarized in Table 1.

2.2. Microstructural characterization

All the samples were prepared for detailed scanning electron microscopy (SEM) and transmission electron microscopy (TEM)

Table 1

Thermal and exposure treatments for the four studied samples.

Sample	Treatments
I	Calcined at 350 °C, air, 2 h
II	Calcined at 350 °C, air, 2 h + fingerprinted
I'	Calcined at 350 °C, air, 2 h + 850 °C, air, 2 h
I''	Calcined at 350 °C, air + 850 °C, air, 2 h + 850 °C, 9% H_2/N_2 , 2 h

investigations. For SEM, fracture surfaces of the samples were used. In order to prepare a high quality cross-section TEM specimen, the samples were first embedded in epoxy to stabilize the porous structure [20] and then mechanically polished to a thickness of approximately 20 μm . Final thinning to <100 nm thickness was done by focused ion beam (FIB) milling at 50 pA probe current using a Carl Zeiss 1540 XB FIB-SEM. The morphology of the sample was analyzed by applying a field-emission gun SEM (Zeiss Supra 35) operated at 5 kV, equipped with backscatter and in-lens detectors and an energy dispersive X-ray spectroscopy (EDX) detector.

A JEM-3000F microscope, equipped with a field-emission gun operated at 300 kV, was employed for transmission electron microscopy (TEM) analysis. The point resolution of the microscope is 0.19 nm. An EDX microanalysis detector with an ultra-thin window was used to perform chemical analysis of samples in scanning transmission electron microscopy (STEM) mode, utilizing a 1 nm probe size; including EDX elemental maps and line scan profiles.

3. Results and discussion

3.1. As-calcined nanoscale infiltrate

The SEM image of the fractured surface of Sample I (see Fig. 1a) shows that after infiltration and subsequent calcination, the CGO/NiO infiltrate existed as a thin connected phase (illustrated by the arrows), homogeneously distributed throughout the backbone, with no detectable preferential coverage of STN or YSZ grains of the backbone. Due to the low volume fraction of YSZ and porous nature of the electrode, it was not possible to directly distinguish STN and YSZ in the composite backbone structure using SEM. Fig. 1b and c shows a TEM image of Sample I and corresponding selected-area electron diffraction (SAED) pattern, respectively. As can be seen from Fig. 1b, the CGO/NiO infiltrates, at a scale of several nanometers, were well distributed on the STN and YSZ grains. As illustrated by the continuous electron diffraction rings of Fig. 1c, the four main crystal planes of a fluorite structure (CaF₂-type CGO), (111), (200), (220) and (311) were identified for the CGO/NiO nanoparticles. Although some species of amorphous nickel oxides might be present on the surface of CGO nanoparticles in Sample I, no crystalline NiO was detected by TEM and SAED. The HRTEM image in Fig. 1d reveals the size of these randomly distributed CGO/NiO nanoparticles to be around 5 nm (see the circled regions). The characteristic (111) crystal plane of CGO was identified for the infiltrated nanoparticles, which is in good agreement with the SAED analysis in Fig. 1c.

3.2. The infiltrate after a fingerprint test

After the fingerprint test, the infiltrate materials changed from CGO/NiO to CGO/Ni due to the reduction of NiO and had coalesced into significantly larger particles, as indicated by the arrows in Fig. 2a. The size of the infiltrates ranged from a few to tens of nanometers, with some being well above 100 nm, as shown by the TEM image in Fig. 2b. The original fluorite infiltrate had grown into distinguishable CGO and Ni phases, as revealed by the SAED analysis in Fig. 2c. In addition to the electron diffraction rings of spots of

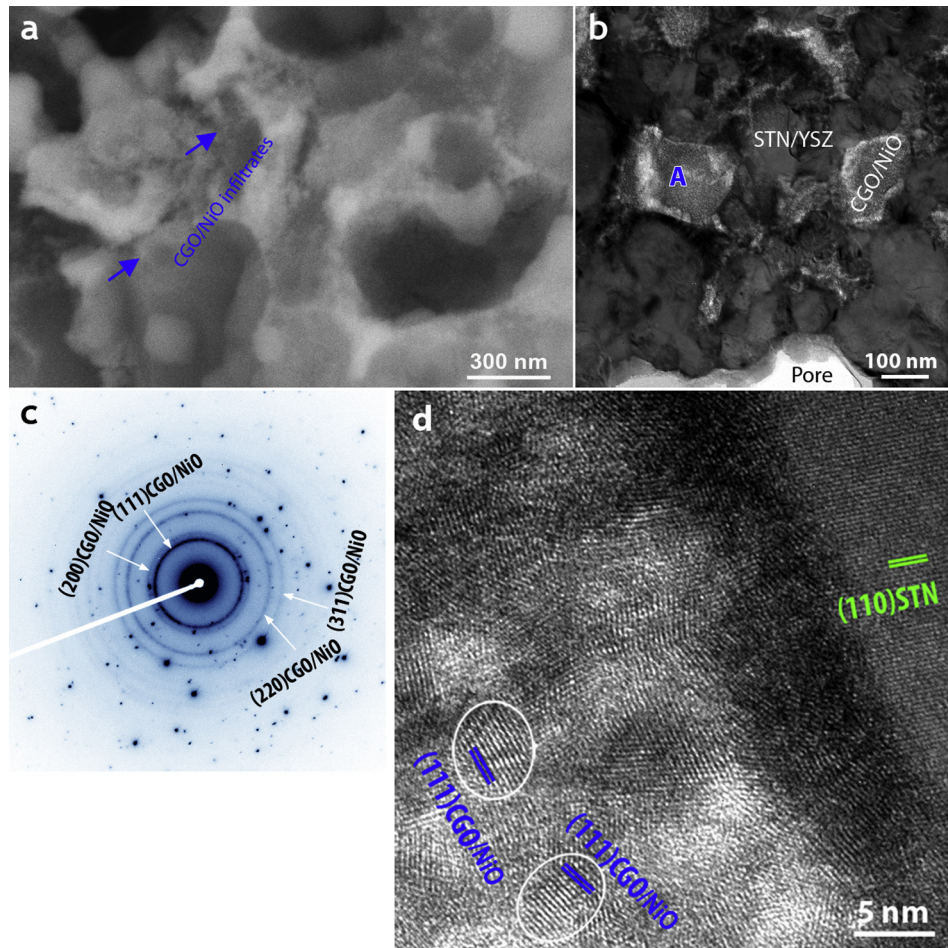


Fig. 1. (a) SEM image of the fractured Sample I. (b) TEM image, (c) SAED pattern and (d) HRTEM image of the infiltration region A in (b).

the CGO phase, which clearly show the growth of CGO nanoparticles, the electron diffraction spots of Ni ((111), (200) and (220) crystal planes) can also now be found.

The HRTEM image of region B of Fig. 2b is shown in Fig. 3a and b. These images show the distribution of CGO and Ni phases by applying the image filtering technique. The two phases appear well connected. Applying the known assumption that the net intensities of peaks in the EDX line scan profiles are roughly proportional to the amount of the elements, ratios between the intensities of the CGO and Ni peaks can be used to obtain further compositional information. As shown in Fig. 3c, the Ce/Gd ratio has a narrow distribution in Sample I, confirming the existence of CGO. The Ni/Ce ratio is always found to be 0.25. This constant ratio indicates that

either Ni can be incorporated into the CGO structure or exists on the CGO phase as amorphous NiO phase. After the electrochemical test, the composition of CGO was unchanged, as indicated by the dominating ratio of Ce/Gd ~ 2.5 in Sample II. However, the ratio of Ni/Ce is spread to a whole range of ratios, revealing that Ni is no longer closely correlated with Ce, which is consistent with Fig. 3b. The CGO (oxide, O) and Ni (metal, M) are observed to be well connected with each other after the test, as shown in Fig. 3d. Through a large amount of EDX line scan profiles of the infiltrated CGO/NiO regions after the test, a particle size distribution was also obtained. Based on the present statistics (see Fig. 3e), the average size of the nanoparticles is ~ 50 nm for both the Ni and CGO phases (Note: grain sizes <20 nm are not counted as they cannot be

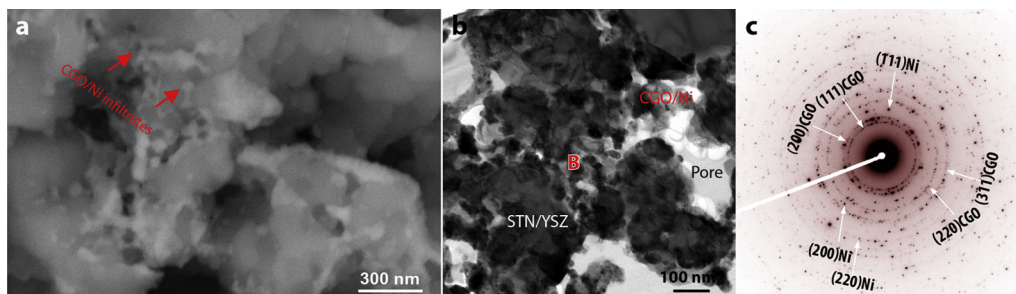


Fig. 2. (a) SEM image of the fractured Sample II. (b) TEM image and (c) SAED pattern of the infiltration region B in (b).

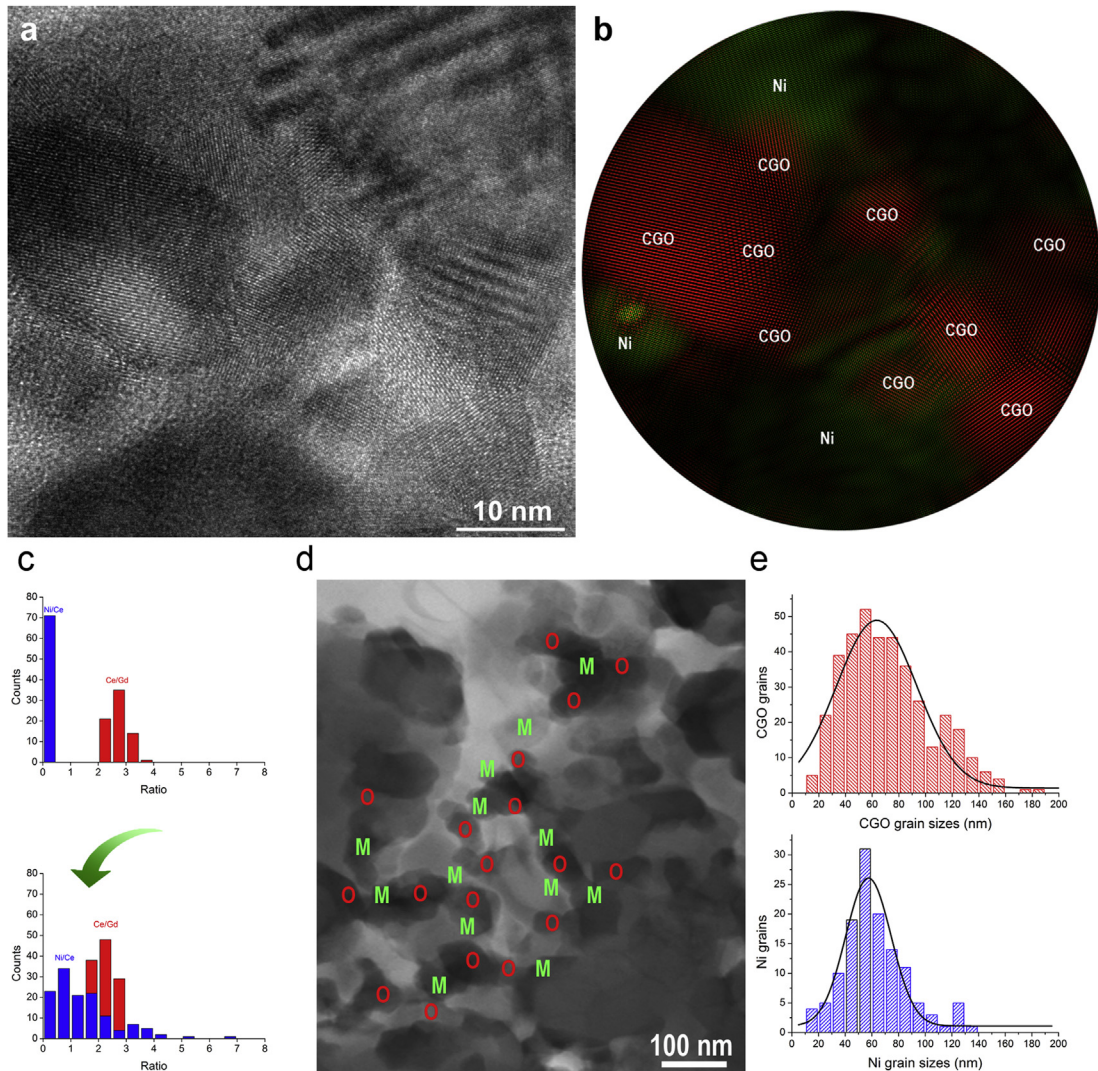


Fig. 3. (a) HRTEM image and (b) the filtered image of the infiltrates in Sample II after the fingerprint test. (c) Histogram of Ce/Gd and Ni/Ce elemental ratios of the infiltrate in (top) Sample I and (bottom) Sample II, obtained from the EDX line scan peaks of Ce, Gd and Ni. (d) BF-STEM images showing the existence of both CGO and Ni phases in Sample II, confirmed by EDX line scan profiles. (e) Histogram of the grain size distributions of (top) CGO and (bottom) Ni phases in Sample II, obtained by using width of the CGO and Ni signals in the EDX line scan profiles.

identified due to the signal to noise ratio); as expected, the amount of CGO grains is higher than that of Ni. Particle growth is usually detrimental as the surface area decreases, thus reducing the amount of electrochemically active sites in an electrode.

3.3. Structural evolution of the infiltrate

Considering that CGO/NiO keeps the fluorite structure of the CGO phase (space group $Fm-3m$, $a = b = c = 5.43 \text{ \AA}$, $\alpha = \beta = \gamma = 90^\circ$) [21], the small amounts of Ni can be incorporated into the CGO lattice in Sample I. This can occur if one of the following ways:

- (1) Ni^{2+} substitutes $\text{Ce}^{4+}/\text{Gd}^{3+}$ in the fluorite structure;
- (2) Ni^{2+} is at the interstitial sites forming a solid solution, particularly the subsurface of the tiny nanoparticles;
- (3) NiO sits on the surface of CGO nanoparticles.

Concerning (1), Thurber et al. [22] reported the substitution of Ni^{2+} for Ce^{4+} , and synthesized the fluorite $\text{Ce}_{0.8}\text{Ni}_{0.2}\text{O}_2$ at 450°C without detection of a NiO phase. Ye et al. [23], from both

microscopy observation and computer simulation, verified that through vacancy compensation, it is possible that Ni can be substitutionally doped into $\text{Ce}_{0.8}\text{Gd}_{0.2}\text{O}_{1.9}$.

In terms of (2), it is possible for Ni to be present in interstitial positions due to the large difference in ionic radius between Ni^{2+} (0.69 \AA) and $\text{Ce}^{4+}/\text{Gd}^{3+}$ ($0.97/0.938 \text{ \AA}$) [24]. According to molecular dynamics simulations [25], in the CaF_2 lattice the presence of Ni^{2+} could be expected at some interstitial sites in the fluorite structure, ascribed to a 29% size difference when comparing Ni^{2+} with Ce^{4+} . Shan et al. observed the formation of fluorite $\text{Ce}_{0.7}\text{Ni}_{0.3}\text{O}_2$ without obvious occurrence of a NiO phase [26].

Thus besides CGO, the fluorites $\text{CeGd}(\text{Ni})\text{O}_x/\text{Ce}(\text{Ni})\text{O}_x$ can also co-exist in the as-calcined infiltrate. However, it is not possible to distinguish them using only SAED analysis and HRTEM imaging, since they do not only keep identical fluorite structures, but also maintain similar lattice parameters although small fluctuations of Ni or Gd exist locally for the CGO/NiO region.

For (3), some tiny species of amorphous nickel oxide can be present on the surface of the CGO nanoparticles in Sample I, although it cannot be detected by using the present analytical

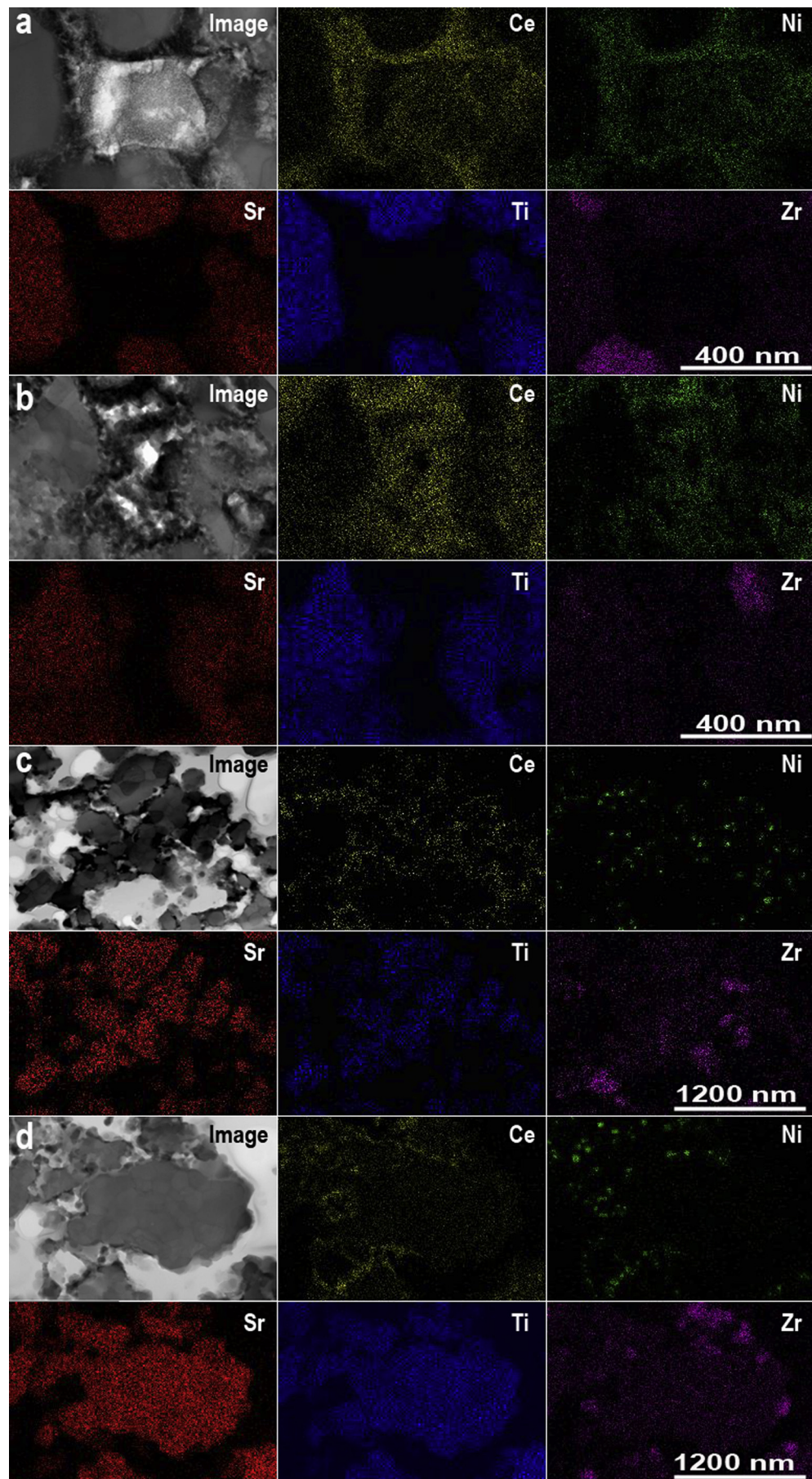


Fig. 4. BF-STEM images and EDX elemental maps (Ce, Ni, Sr, Ti and Zr) of Samples I (a), I' (b), I'' (c) and II (d), respectively.

methods. It was found that such dispersed NiO has strong interaction with cerium oxide [26]. Wrobel et al. [27] pointed out that the strong interactions between Ce and Ni species occurred in the NiO–CeO₂ solid solution and/or at the interface of amorphous NiO/ceria, and that the solid solution can be formed at the interface between NiO and ceria.

Based on the aforementioned analysis, we have observed the indistinguishable CGO/Ni fluorite structure in the as-calcined Sample I.

A detailed compositional analysis of the samples was conducted to probe the structural evolution of the infiltrates. Fig. 4a shows the EDX elemental maps of Sample I, where the five main elements were chosen, Ce and Ni representing the infiltrate, Sr and Ti representing STN, and Zr representing YSZ. One can find that the Ce and Ni signals are correlated in the whole analyzed region in terms

of both location and intensity. As shown in Fig. 5a, the line profile of Ni is closely correlated with that of Ce, coinciding also with Gd (see the arrows).

Sample I' underwent a stay in air at 850 °C for 2 h, after an initial calcination at 350 °C for 2 h in air. This is a high-temperature sintering environment, which facilitated the growth of the nanoscale CGO/NiO nanoparticles, as shown by the image in Fig. 4b. The particles grew up to 10–20 nm. No significant change can be detected for the distribution of Ce and Ni in the infiltrate. As illustrated in Fig. 5b, the line profile of Ni is still approximately correlated with that of Ce, coinciding also with Gd (see the arrows). The local fluctuation of Ni and Gd can be found, as the high-temperature sintering has induced growth of CGO/NiO infiltrate to some extent consisting of Ni-containing CGO and NiO phases, as shown in Fig. 6a and b.

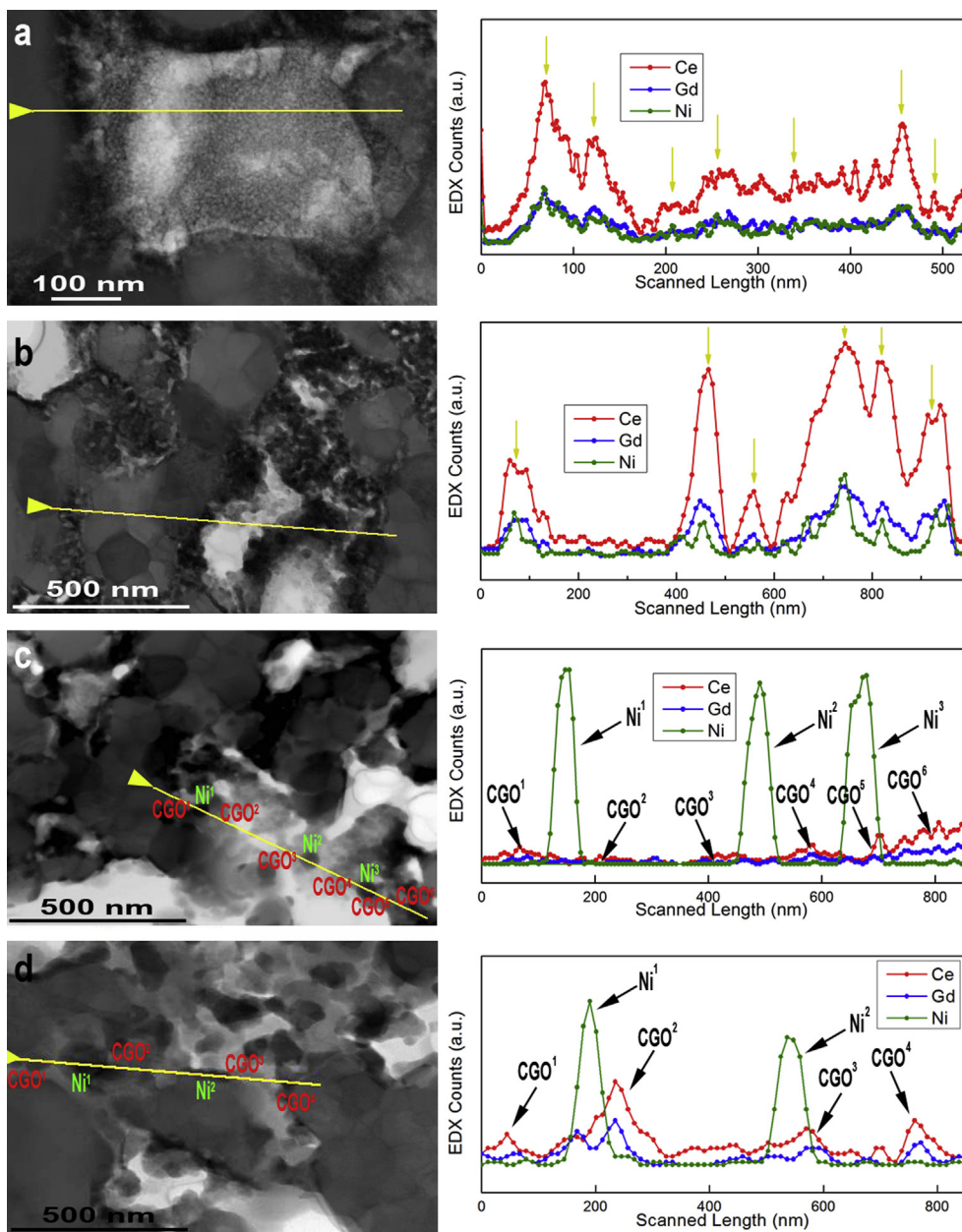


Fig. 5. BF-STEM images and the corresponding EDX line profiles (Ce, Gd and Ni) of Samples (a) I, (b) I', (c) I'' and (d) II, respectively. In (a) and (b), the arrows show the elemental correlation at some particular locations.

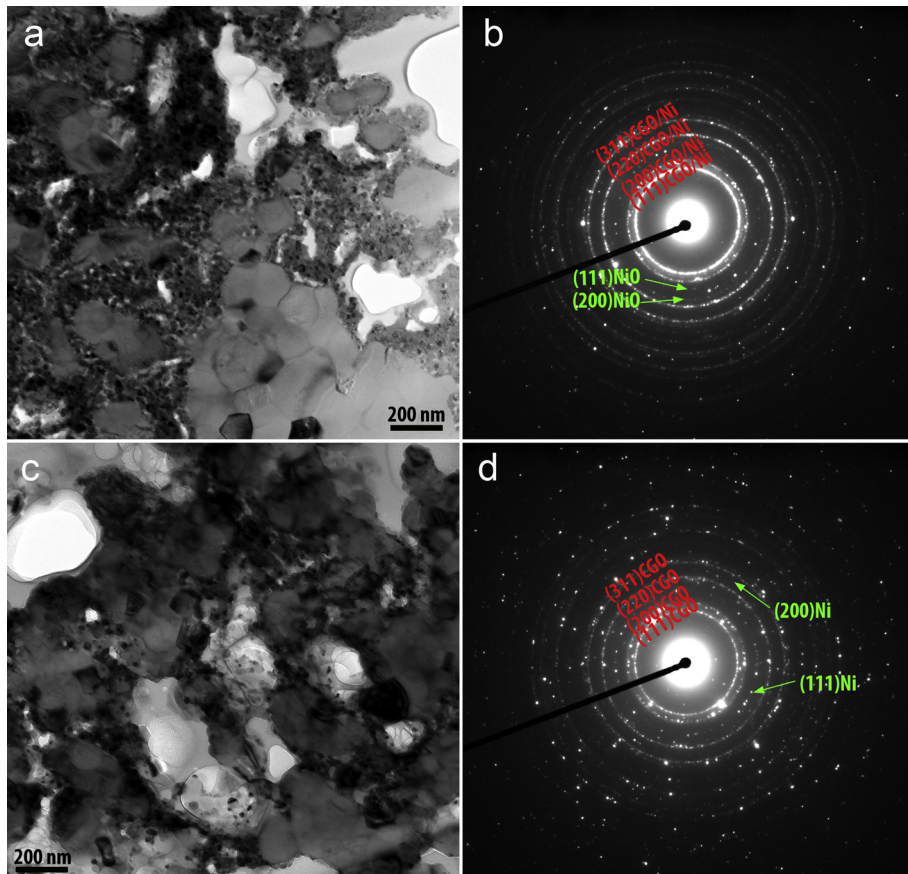


Fig. 6. (a) TEM image and (b) SAED patterns of the infiltration in Sample I'. (c) TEM image and (d) SAED patterns of the infiltration in Sample I''.

Further treatment of Sample I' at 850 °C in H₂/N₂ atmosphere for 2 h, resulted in the significant infiltrate growth on the backbone of Sample I'', as shown by Fig. 4c. At this scale a significant enhancement of intensities of individual Ni locations can be seen comparing Ce and Ni. As shown in Fig. 5c, the strong correlation between Ce and Ni seen for the Sample I has been totally lost. Thus, compositional analysis corroborates the existence of individual CGO and Ni phases. The CGO and Ni phases are alternating along the scanned lines, i.e., CGO¹, Ni¹, CGO², CGO³, Ni², CGO⁴, Ni³, CGO⁵ and CGO⁶. The large difference of contrast in image and intensity in the corresponding profile illustrates that in contrast to the grown Ni grain that reduced from the Ni-containing CGO and/or surface NiO, the remaining CGO region has not been well grown and existed as the thin covering layers. That is to say, the brief high-temperature reduction seems to have a significant impact on the Ni growth, but very limited impact for the CGO. Fig. 6 shows the morphology and SAED analysis of the grown infiltrate.

With the introduction of extending testing in H₂O/H₂, the CGO particles have also grown to a similar size as the Ni particles in Sample II, as illustrated by the particle size distribution in Fig. 3e. Comparing with Sample I', as shown by Fig. 5d, the enhancement of intensities of individual Ni particles is more pronounced. In Fig. 5d, one can find that the CGO and Ni phases are alternatingly distributed along the scanned lines, CGO¹, Ni¹, CGO², Ni², CGO³ and CGO⁴. The impact of high steam partial pressure can be favorable for the Ni growth [28,29]. It was reported that self-limiting grain growth for CGO nanoparticles occurred upon exposure to a temperature below 1100 °C, and the average particle size was below 140 nm [30]. The formed Ni clusters will undergo local surface

diffusion followed by its coalescence or agglomeration, as Ni has a high self-diffusion coefficient at elevated temperature [31,32]. But limiting growth of Ni also exists in Sample II. In the presence of steam, Ni(OH)₂ formation may result also in Ni transport via the gas-phase at the sites of local higher oxygen activity, followed by Ni recondensation when Ni(OH)₂ is again reduced at the sites of local lower oxygen activity [33], which will limit the growth of Ni. Due to the nanoparticle growth and morphology change, loss of catalytic activity of the electrocatalysts occurred and a complicated degradation of electrochemical properties were demonstrated in our previous work [18,19].

4. Conclusion

A detailed microstructural investigation was performed on CGO/Ni infiltrated STN/YSZ electrodes that had been tested in a symmetric cell design under a variety of H₂O/H₂ conditions. The instability and growth behavior of the CGO/Ni infiltrate was revealed as follows. The 5 nm CGO/Ni particles exist as a fluorite structure in the low temperature (350 °C) calcined sample. Clear phase separation into CGO and NiO was not observed with the used techniques. After treatment in air at 850 °C for 2 h, the particles have grown to 10–20 nm. After a further treatment at 850 °C in H₂/N₂ atmosphere for 2 h, both CGO and Ni phases can be clearly identified. The brief high-temperature reduction can have a significant impact on the Ni growth (grew from 5 to 50 nm), but very limited impact on the CGO. After a more extended exposure and electrochemical characterization test, the CGO/Ni infiltrate evolved into well-separated CGO and Ni phases, with an average size up to 50 nm.

Acknowledgments

This research has received funding from the European Union's Seventh Framework Programme (FP7/2007–2013) for the Fuel Cells and Hydrogen Joint Technology Initiative under grant agreement n° 256730. The authors wish to thank Dr. Peter Holtappels and Dr. Peter Blennow for useful discussions and Mrs. Ebtisam Abdellahi for TEM sample preparations. Furthermore the authors would like to thank Guoyu Zhang, Mr. Shiyang Cheng, Dr. Finn W. Poulsen, Dr. Mohammed Hussain, Dr. Jacob R. Bowen and Dr. Ming Chen for their help.

References

- [1] E.D. Wachsman, K.T. Lee, *Science* 334 (2011) 935–939.
- [2] T. Suzuki, Z. Hasan, Y. Funahashi, T. Yamaguchi, Y. Fujishiro, M. Awano, *Science* 325 (2009) 852–855.
- [3] P. Holtappels, B.R. Sudireddy, in: R. Riedel, I.-W. Chen (Eds.), *Ceramics Science and Technology Volume 4: Applications*, Wiley-VCH, 2013.
- [4] W.C. Chueh, Y. Hao, W. Jung, S.M. Haile, *Nat. Mater.* 11 (2012) 155–161.
- [5] S.P. Jiang, *Mater. Sci. Eng. A* 418 (2006) 199–210.
- [6] S.P. Jiang, *Int. J. Hydrogen Energy* 37 (2012) 449–470.
- [7] M. Mogensen, N.M. Sammes, G.A. Tompsett, *Solid State Ionics* 129 (2000) 63–94.
- [8] U.P. Muecke, S. Graf, U. Rhyner, L.J. Gauckler, *Acta Mater.* 56 (2008) 677–687.
- [9] R. Knibbe, H.-J. Wang, P. Blennow, K. Thydén, Å.H. Persson, L. Mikkelsen, T. Klemmø, *J. Power Sources* 228 (2013) 75–82.
- [10] C. Bernuy-Lopez, R. Knibbe, Z. He, X. Mao, A. Hauch, K.A. Nielsen, *J. Power Sources* 196 (2011) 4396–4403.
- [11] A.M. Hussain, J.V.T. Høgh, W. Zhang, N. Bonanos, *J. Power Sources* 216 (2012) 308–313.
- [12] P.R. Shearing, D.J.L. Brett, N.P. Brandon, *Int. Mater. Rev.* 55 (2010) 347–363.
- [13] W. Zhang, M. Chen, L. Theil Kuhn, J.R. Bowen, J.J. Bentzen, *ChemElectroChem* (2014), <http://dx.doi.org/10.1002/celec.201300045>.
- [14] J. Canales-Vázquez, S.W. Tao, J.T.S. Irvine, *Solid State Ionics* 159 (2003) 159–165.
- [15] O.A. Marina, N.L. Canfield, J.W. Stevenson, *Solid State Ionics* 149 (2002) 21–28.
- [16] B.R. Sudireddy, P. Blennow, K.A. Nielsen, *Solid State Ionics* 216 (2012) 44–49.
- [17] P. Blennow, K.K. Hansen, L.R. Wallenberg, M. Mogensen, *Solid State Ionics* 180 (2009) 63–70.
- [18] T. Ramos, C. Bernuy-Lopez, B.R. Sudireddy, J.J. Bentzen, W. Zhang, P.S. Jørgensen, L. Theil Kuhn, *ECS Trans.* 45 (2012) 389–402.
- [19] T. Ramos, S. Veltzé, B.R. Sudireddy, P. Holtappels, *ECS Electrochem. Lett.* 3 (2014) F5–F6.
- [20] W. Zhang, L. Theil Kuhn, P.S. Jørgensen, K. Thydén, J.J. Bentzen, E. Abdellahi, B.R. Sudireddy, M. Chen, J.R. Bowen, *Microsc. Microanal.* 19 (2013) 501–505.
- [21] M. Swanson, M. Sunder, N. Tangtrakarn, L. Krishna, P.D. Moran, *Solid State Ionics* 189 (2011) 45–49.
- [22] A. Thurber, K.M. Reddy, V. Shutthanandan, M.H. Engelhard, C. Wang, J. Hays, A. Punnoose, *Phys. Rev. B* 76 (2007) 165206.
- [23] F. Ye, T. Mori, D.R. Ou, J. Zou, J. Drennan, S. Nakayama, M. Miyayama, *Solid State Ionics* 181 (2010) 646–652.
- [24] R.D. Shannon, *Acta Crystallogr. A* 32 (1976) 751–767.
- [25] D. Zahn, P. Heitjans, J. Maier, *Chem. Eur. J.* 18 (2012) 6225–6229.
- [26] W. Shan, M. Luo, P. Ying, W. Shen, C. Li, *Appl. Catal. A* 246 (2003) 1–9.
- [27] G. Wrobel, M.P. Sohier, A. D'Huysser, J.P. Bonnelle, *Appl. Catal. A* 101 (1993) 73–93.
- [28] A. Hauch, M. Mogensen, A. Hagen, *Solid State Ionics* 192 (2011) 547–551.
- [29] J. Sehested, J.A.P. Gelten, S. Helveg, *Appl. Catal. A* 309 (2006) 237–246.
- [30] J.L.M. Rupp, A. Infortuna, L.J. Gauckler, *Acta Mater.* 54 (2006) 1721–1730.
- [31] M. Mogensen, S. Skaarup, *Solid State Ionics* 86–88 (1996) 1151–1160.
- [32] M.M. Murphy, J. Van Herle, A.J. McEvoy, K.R. Thampi, *J. Electrochem. Soc.* 141 (1994) L94–L96.
- [33] A. Grubner, in: *SOFCE V Proceedings*, Electrochemical Society, Pennington, NJ, 1997, pp. 844–850.